Theory of Angle Resolved Photoemission Spectroscopy of Altermagnetic Mott Insulators

Lorenzo Lanzini,[1,2,*] Purnendu Das,[3,1,2] and Michael Knap[1,2]
[1]Technical University of Munich, TUM School of Natural Sciences, Physics Department, 85748 Garching, Germany
[2]Munich Center for Quantum Science and Technology (MCQST), Schellingstrasse 4, 80799 München, Germany
[3]Indian Institute of Science, Bangalore, 560012, India

(Received 9 June 2025; revised 13 November 2025; accepted 16 June 2026; published 28 July 2026)

Altermagnetism has emerged as an unconventional form of collinear magnetism with spatial rotational symmetries, that give rise to strongly spin-split bands despite an underlying fully compensated antiferromagnetic order. Here, we develop a theory for the angle resolved photoemission spectroscopy response of altermagnetic Mott insulators. Crucially, the spectrum does not simply reflect the noninteracting band structure, but instead a magnetic polaron is formed at low energies, that can be interpreted as a spinon-holon bound state. We develop a spinon-holon parton theory and predict a renormalized bandwidth that we confirm by tensor network simulations. We analyze the characteristic spin-split spectrum and identify a spin-dependent spectral weight of the magnetic polaron, resulting from the altermagnetic symmetry. Our Letter paves the way for a systematic study of doping effects and correlation phenomena in altermagnetic Mott insulators.

DOI: 10.1103/1d1n-cssv

Introduction—Altermagnets are collinear magnets, that in some respect are distinct from ferromagnets and from conventional antiferromagnets [1,2]. Although altermagnets have zero net magnetization resembling antiferromagnets, an underlying rotational symmetry between the sublattices gives rise to spin-split bands [1–34]. The spin splitting can be directly probed by angle resolved photoemission spectroscopy (ARPES) [35]. Recently (spin-resolved) ARPES and other spectroscopic probes have been measured for a range of altermagnetic candidate materials [36–43]. For instance, a very strong spin-split band structure has been observed in the weak insulator MnTe [36–38,44–48]. Many altermagnetic materials have also been argued to be strongly correlated Mott insulators [49–51], where the Coulomb repulsion causes strong localization of electrons. Among them is the recently discovered $La_2O_3Mn_2Se_2$, a Mott insulating layered material exhibiting d-wave altermagnetism [52,53].

The ARPES response should be interpreted as a measure of the dynamics of charge dopants injected into the altermagnet. In general, these dopants do not reflect the bare band structure of the material, but instead a magnetic polaron is formed due to interaction with the magnetic environment [54–60]. For conventional antiferromagnets, an intuitive picture capturing the magnetic polaron formation is obtained from a parton description in which the doped hole splits into a spinon and a holon [57,61–67]. In this picture, the magnetic polaron is a quasiparticle that is a bound state of the fast holon and the slow spinon. Despite the wealth of recent ARPES experiments, the consequences of the magnetic polaron formation in altermagnetic insulators have not been investigated thus far.

In this Letter, we determine the spin-resolved ARPES response of a d-wave altermagnetic Mott insulator [15] using tensor network methods and develop a parton theory [63] for the magnetic polaron formation; see Fig. 1. Our theory predicts a strong renormalization of the quasiparticle bandwidth due to interactions with the antiferromagnetic background, however, in a more complex way compared to simple square-lattice antiferromagnets. We determine the characteristic spin splitting of the bands and analyze the spin-anisotropic spectral weight of the magnetic polaron, that we argue are key signatures of altermagnetism.

The altermagnetic Mott insulator—We consider an altermagnetic Hubbard model on a square lattice $\hat{H} = -\sum_{i,j,\sigma} t_{ij}(c^{\dagger}_{i\sigma}c_{j\sigma} + \text{H.c.}) + U\sum_i n_{i\uparrow}n_{i\downarrow}$, where $c_{i\sigma}$ ($c^{\dagger}_{i\sigma}$) are the fermionic annihilation (creation) operators [15]. The hopping matrix elements are $t_{ij} = t$ for nearest neighbors, while $t_{ij} = t_+$ in the $\boldsymbol{a}_1 = (1,1)$ direction for the A sublattice and in the $\boldsymbol{a}_2 = (-1,1)$ direction for the B sublattice, and zero for all the other bonds; see Fig. 1(a). This model has an altermagnetic $\pi/2$ symmetry (d-wave symmetry), expected to capture, e.g., the Mn_2O layers in $La_2O_3Mn_2Se_2$ [52,53].

*Contact author: lorenzo.lanzini@polytechnique.edu

Published by the American Physical Society under the terms of the Creative Commons Attribution 4.0 International license. Further distribution of this work must maintain attribution to the author(s) and the published article's title, journal citation, and DOI.

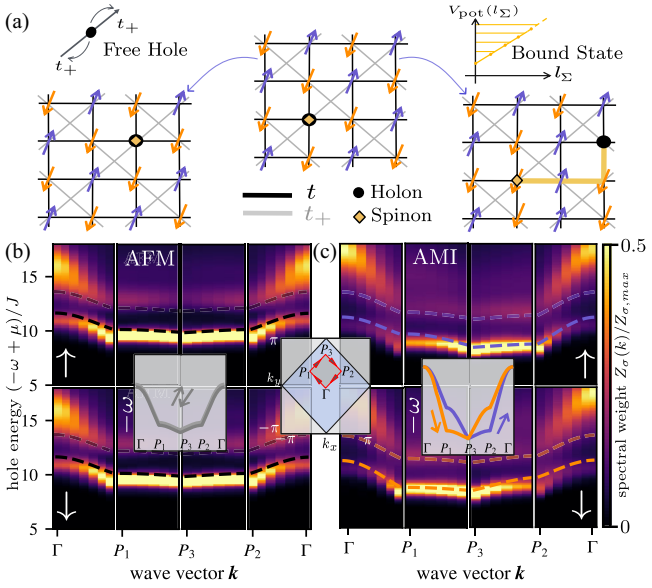


FIG. 1. The altermagnetic polaron. (a) Center: a hole doped into an altermagnetic Mott insulator with Néel order can be interpreted as a tightly bound spinon (diamond) and holon (circle). Two main processes contribute to the dynamics. Left: anisotropic diagonal hopping t_+ of the spinon-holon composite that retains the Néel order; Right: nearest-neighbor hopping t that displaces the magnetic background and thus generates an effective confining potential for the spinon and holon. Spin-resolved ARPES response (top spin, ↑; bottom spin, ↓), in (b) the antiferromagnet (AFM) and (c) the altermagnetic Mott insulator (AMI), obtained with tensor network simulations for $t_+/t = 0.4, t/J = 3$ (color plot) compared with the parton theory (dashed lines). Both cases show a quasiparticle peak—the magnetic polaron—at low energies. Such peak is characterized by a strongly reduced bandwidth [$W \sim \mathcal{O}(J)$ with respect to the bandwidth at the mean-field level $W \sim \mathcal{O}(t)$]. While for the AFM the spectra are spin symmetric [cf. inset of (b)], for the AMI they are anisotropic and are related by the altermagnetic $\pi/2$ symmetry of the model [cf. inset of (c)]. In both AFM and AMI spectra, a higher energy vibrational peak of the magnetic polaron is observed (faint dashed line).

In the limit of strong interactions ($U \gg t$), we project out double occupancies using a Schrieffer-Wolff transformation to obtain an effective $t-J$ model:

$$\mathcal{H} = \sum_{ij,\sigma} -t_{ij}(\mathcal{P}_G c^\dagger_{i\sigma} c_{j\sigma} \mathcal{P}_G + \text{H.c.}) + J_{ij}\left(\boldsymbol{S}_i \cdot \boldsymbol{S}_j - \frac{n_i n_j}{4}\right), \quad (1)$$

where $J_{ij} = 4t_{ij}^2/U$ are the spin-exchange couplings and $\mathcal{P}_G$ is a Gutzwiller projection to the single occupied local basis states. Third-order terms involving three sites on a triangle vanish for real hopping [68]. The spin excitations of insulating altermagnets in the absence of doping have been analyzed recently, see e.g., Refs. [69,70]. Here, we focus on the single-particle spectral function that is measured in ARPES experiments.

Single-particle spectral function—In order to numerically compute the single-particle spectral function for large systems, we first perform tensor network simulations to determine the ground state $|\Psi_0\rangle$ of model (1) at half filling. We add a weak sublattice potential to break the SU(2) symmetry of the model and to spontaneously form Néel order. We represent the wave function as a matrix product state on elongated cylinder geometries and variationally optimize the ground state with the Density Matrix Renormalization Group (DMRG) algorithm [71] using the TeNPy package [72]. We then compute the time-dependent correlation function $\langle\Psi_0|c^\dagger_{\boldsymbol{r}_b\sigma}(\tau)c_{\boldsymbol{0}_a\sigma}|\Psi_0\rangle$, where the indices a, b of the real space coordinates indicate the position in the two-site unit cell and τ is real time. From this correlation function, we obtain the spin-resolved spectral function

$$A_\sigma(\mathbf{k},\omega) = \sum_{a,b}\int \mathrm{d}\mathbf{r}_b \mathrm{d}\tau e^{i(\tau\omega - \mathbf{k}\mathbf{r}_b - k_y(b-a))} \times \langle\Psi_0|c^\dagger_{\boldsymbol{r}_b\sigma}(\tau)c_{\boldsymbol{0}_a\sigma}|\Psi_0\rangle, \quad (2)$$

measured with spin-resolved ARPES.

We now determine the spin-resolved spectral function both for the square-lattice antiferromagnet $t = 3J, t_+ = 0$ and the altermagnet $t = 3J, t_+ = 0.4t$; see Figs. 1(b) and 1(c). We have introduced a small staggering field $B = 5\times10^{-3}J$ to the Hamiltonian to break the spin symmetry in the z direction, resulting in a staggered magnetization $m \simeq 0.25$, which is half of the saturated Néel order. This reduction is due to the strong quantum fluctuations that in 2D reduce the Néel order parameter. It is consistent with a linear spin-wave analysis of the Heisenberg model; see the Supplemental Material [73], which includes Ref. [74]. We consider cylinder geometries elongated in the $\boldsymbol{a}_1(\boldsymbol{a}_2)$ direction, leading to a fine resolution of the shown Brillouin zone cuts. We determine the chemical potential by calculating the DMRG energies with $N+1$ and $N-1$ electrons, $\mu_{hf} = [E(N+1) - E(N-1)]/2$, such that the Mott gap can be directly read off from the spectra [75]. The numerical results obtained from the tensor network simulations are checked to be converged with the bond dimension of the matrix product state, which is the control parameter for the accuracy of the simulations; see the Supplemental Material for a detailed analysis [73], which includes Ref. [76]. Comparing the antiferromagnet and the altermagnet, both show a well-defined quasiparticle peak at low energies, indicating the formation of the magnetic polaron. We further find the minimum of the dispersion both for the altermagnet and the antiferromagnet at the nodal point $Q_2 = (\pi/2, \pi/2)$.

Crucially, we also identify key differences between the antiferromagnet and the altermagnet. First, the antiferromagnet has spin degenerate bands while the altermagnet does not. In particular, the bands in the altermagnet are spin split, and the spectra are related by a $\pi/2$ rotation expected

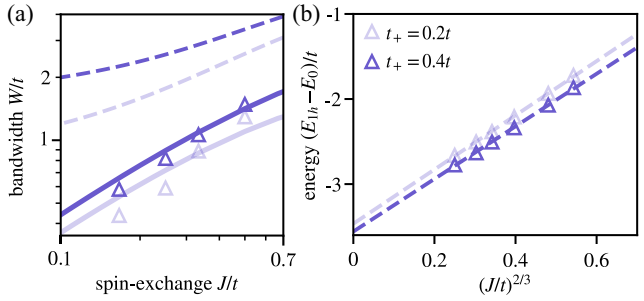


FIG. 2. Signatures of the polaron formation. (a) Bandwidth of the altermagnetic polaron extracted from the spectral function, that we compute with tensor networks (triangles), compared with the parton theory (solid lines). The bandwidth W of the polaron is strongly renormalized compared to the Hartree-Fock prediction (dashed lines). (b) Energy difference of the single-hole and the undoped ground state (triangles), which we find to scale as $\sim(J/t)^{2/3}$ (dashed line), suggesting the formation of a linear confinement potential between the holon and the spinon.

for the d-wave altermagnet of Eq. (1). Second, in the altermagnet the spectral weight is not uniform for the two spin orientations, which we propose as an additional experimental signature of altermagnetic Mott insulators.

We now determine the single-particle spectral function for various values of the spin exchange J and diagonal hoppings t_+ and extract the bandwidth W of the magnetic polaron; see Fig. 2(a). The bandwidth W increases with spin exchange J and with diagonal hopping t_+; however, it is strongly reduced compared to the Hartree-Fock prediction, hinting at a strong renormalization of the doped hole. To gain further understanding of the structure of the state, we compute the energy difference of the ground state at half filling and the one with a doped hole. We find that this energy difference scales as $\Delta E/t \propto (J/t)^{2/3}$ [see Fig. 2(b)], reminiscent of the polaron formation in the conventional square-lattice antiferromagnet [64,77,78].

Microscopic spinon-holon parton theory—In our tensor network simulations we observed a strong renormalization of the magnetic polaron by the magnetic background. In order to interpret this process, we develop a parton theory [64,65], in which the fermionic hole fractionalizes into a heavy spinon that carries the spin quantum number and a light bosonic holon that carries the charge; see Fig. 1(a). Qualitatively, two distinct processes can arise for a square lattice antiferromagnet with both nearest and next-nearest neighbor hopping. On the one hand, the diagonal hopping leaves the Néel ordered background invariant and the spinon and holon remain tightly bound (left panel). On the other hand, the nearest-neighbor hopping leads to a separation of the light holon and the heavy spinon, creating geometric strings of displaced spins (right panel). The properties of the displaced strings can be evaluated using a Born-Oppenheimer type approximation, in which the hole does not change the quantum state or entanglement but only displaces spins, which is referred to as frozen spin approximation (FSA) [63,79,80].

We consider the ground state $|\Psi_0\rangle$ at half filling and dope a hole at position $\boldsymbol{j}^s$. The state is denoted as $|\boldsymbol{j}^s,\bar{\sigma},0\rangle = c_{\boldsymbol{j}^s,\sigma}|\Psi_0\rangle$. We decompose the hole into partons: a holon $h_j^\dagger$ and a spinon $f_{j,\sigma}$, i.e., $c_{\boldsymbol{j}^s,\sigma} = h_j^\dagger f_{j,\sigma}$. In the basis state $|\boldsymbol{j}^s,\bar{\sigma},0\rangle$ the spinon is therefore located at position $\boldsymbol{j}^s$ and has spin $\bar{\sigma} = -\sigma$. The motion of the holon creates different geometric strings Σ of the displaced spins, $|\boldsymbol{j}^s,\bar{\sigma},\Sigma\rangle$, keeping the spinon position fixed. The spinon and the holon are connected by strings of displaced spins; each of them comes at an energy cost. Thus separating the spinon and the holon leads to a potential $V_{\mathrm{pot}}(\Sigma)$ that grows linearly with the length of the string Σ. In that picture of frozen spins, the holon motion can be modeled as a single particle hopping problem on the Bethe lattice with linearly increasing potential (see End Matter for details). This linear dependence on string length effectively gives rise to a spinon-holon bound state of energy $E_{\mathrm{FSA}} \sim (J/t)^{2/3}$ in agreement with the numerical results; see Fig. 2(a). The bound state is given by a superposition of all strings $|\psi_{\mathrm{FSA}}(\boldsymbol{j}^s,\bar{\sigma})\rangle = \sum_\Sigma \psi_\Sigma^{\mathrm{FSA}}|\boldsymbol{j}^s,\bar{\sigma},\Sigma\rangle$, and can be computed numerically by solving the Bethe lattice Hamiltonian. From that we obtain the probability distribution $p_\Sigma^{\mathrm{FSA}} = |\psi_\Sigma^{\mathrm{FSA}}|^2$ for a geometric string Σ. Crucially, compared to the conventional antiferromagnet, the diagonal hopping processes renormalize the probability of strings of zero length; see the Supplemental Material [73].

The motion of the fast holon that we discussed so far assumes the position of the slow spinon to be fixed. This yields a dispersionless contribution coming from the fluctuating geometric strings. However, the spinon has a finite energy scale, and we now analyze the slow dynamics of the spinon that determines the entire dispersive part as well as the spin-split nature of the spectral function. For zero string length the holon and spinon are bound together, and both can hop diagonally without any energy cost, effectively contributing to the dispersive nature of the spectral function, by $E_{t_+}^{\mathrm{bare}}(\boldsymbol{k},\sigma) = 2t_+|\psi_0^{\mathrm{FSA}}|^2(\cos k_1\delta_{\sigma\uparrow} + \cos k_2\delta_{\sigma\downarrow})$ where $k_1 = k_x + k_y$ and $k_2 = k_y - k_x$. This is the primary contribution to the spin anisotropy characteristic for altermagnetic states.

For strings Σ of finite length, the spin-exchange coupling governs the motion of the spinon, which in terms of spinons reads as $\boldsymbol{S}_i \cdot \boldsymbol{S}_j = \frac{1}{2}(f_{i\uparrow}^\dagger f_{i\downarrow} f_{j\downarrow}^\dagger f_{j\uparrow} + \mathrm{H.c.}) + \frac{1}{4}(n_{i\uparrow} - n_{i\downarrow})(n_{j\uparrow} - n_{j\downarrow})$. We consider all the possible spinon exchanges around the spinon at the state $|\boldsymbol{j}^s,\bar{\sigma},\Sigma\rangle$. The spinon exchanges that involve nearest neighbor sites gives a contribution $E_J(\boldsymbol{k}) = J\nu_{\mathrm{FC}}^{(1)}[A(\cos k_1 + \cos k_2) + B(\cos 2k_x + \cos 2k_y)]$ where nearest-neighbor couplings are renormalized by the Franck-Condon factor $\nu_{\mathrm{FC}}^{(1)} = \sum_{\Sigma,\Sigma'|\Sigma} \psi_\Sigma^{\mathrm{FSA}}\psi_{\Sigma'}^{\mathrm{FSA}}$, where the summation $\Sigma'|\Sigma$ is taken over all new strings Σ' that result

from the original string Σ after a spinon exchange; the prefactors are $A = 8/3, B = 3/2$; see the Supplemental Material [73]. In the conventional antiferromagnetic $t-J$ model, this contribution gives a spin-degenerate dispersion [64,65]. However, in our model, spinon exchanges occur also along the diagonal for which $J_{ij} = J_+$ gives rise to $E_{J_+}(\boldsymbol{k},\sigma) = J_+\nu_{\mathrm{FC}}^{(2)}(\cos k_1\delta_{\sigma\uparrow} + \cos k_2\delta_{\sigma\downarrow})$, yielding a spin-split dispersion that is renormalized by the Franck-Condon factor $\nu_{\mathrm{FC}}^{(2)} = (1 - |\psi_0^{\mathrm{FSA}}|^2)$.

In summary, the resulting momentum-dependent energy of the magnetic polaron is

$$E(\boldsymbol{k},\sigma) = J\nu_{FC}^{(1)}[A(\cos k_1 + \cos k_2) + B(\cos 2k_x + \cos 2k_y)] + (J_+\nu_{FC}^{(2)} + 2t_+|\psi_0^{\mathrm{FSA}}|^2)(\cos k_1\delta_{\sigma\uparrow} + \cos k_2\delta_{\sigma\downarrow}) + E_{\mathrm{FSA}}. \quad (3)$$

We show the thus obtained spinon dispersion both for the antiferromagnetic and the altermagnetic case in Figs. 3(a) and 3(b), respectively. For the antiferromagnet, the magnetic polaron is spin degenerate. By contrast, for the altermagnet we observe a strong spin splitting, lifting the degeneracy of global minima at the nodal points $Q_1 = \pm(-\pi/2, \pi/2)$ $Q_2 = \pm(\pi/2, \pi/2)$ for spin $\uparrow$ ($\downarrow$). Our theory predicts that the dominant contribution to the spin splitting arises from the rescaled free-hole contribution, $E_{t_+}^{\mathrm{bare}}$.

We now analyze the renormalization of the band structure due to the polaron formation in more detail. To this end, we first compute the self-consistent mean-field Hamiltonian of the altermagnetic Hubbard model in the Mott insulating regime and determine the excitation spectrum, following Ref. [15]; see dashed line in Fig. 3(b). The correct polaron dispersion obtained from the parton theory, however, is strongly renormalized to lower energies due to the interactions with the magnetic background [solid lines in Fig. 3(b)]. This highlights the strong interaction effects, that are relevant for forming the altermagnetic polaron.

We also compare the altermagnetic polaron dispersion obtained analytically from the spinon-holon parton theory determined with the numerical results for the spectral function [dashed lines in Fig. 1(c)]. For a consistent comparison, we recomputed the FSA ground state energy (E_{FSA}) using DMRG correlations in the FSA potential energy of strings, rather than the Néel state (see the Supplemental Material [73]). This adjustment allows us to reproduce the tensor network energy shift in our simple parton theory, resulting in excellent agreement between the numerical results and the analytical prediction for all momenta, and highlighting the importance of quantum fluctuations.

The spin-splitting of the altermagnetic polaron leads to a transfer of spectral weight between spin polarizations; see

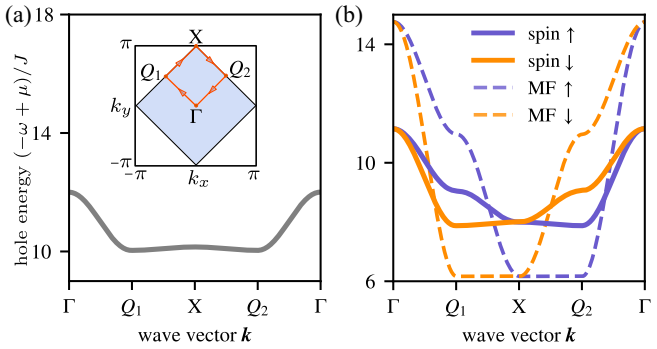


FIG. 3. Parton description of the polaron dispersion. Predicted dispersion of the magnetic polaron based on a spinon-holon parton approach (solid lines) for (a) the AFM with $t_+ = 0$ and (b) the AMI with $t_+ = 0.4t$, evaluated along the Brillouin zone cut shown in the inset of (a). The AFM hosts spin-degenerate bands, while the AMI has an anisotropic spin splitting that governs the rotational symmetry of the d-wave altermagnet. Mean-field energy bands ($U = 12t, t_+ = 0.4t$) were obtained from Hartree-Fock as described in [15] (dashed lines).

Fig. 1(c). We determine the spectral weight $Z(\boldsymbol{k})$ of the polaron branch at $\boldsymbol{k} = (k_1, 2\pi/3)$ by extracting the half width at half maximum from the spectral function, numerically obtained from tensor network simulations; see Fig. 4(a). While for this cut in the Brillouin zone the spectral weight is approximately constant for the antiferromagnet, the situation for the altermagnet is more involved. For spin $\uparrow$, which for the given Néel order is mainly subjected to diagonal hopping in the $\boldsymbol{a}_1$ direction, the spectral weight peaks at $\boldsymbol{k} = (k_1 = \pi, 2\pi/3)$ (P_4). By contrast, the weight for spin $\downarrow$ is weakly dependent on momentum. The transfer of spectral weight results from an interference effect of the single-particle hopping on the lattice along with the spontaneous formation of Néel order, which we demonstrate by computing the quasiparticle weight of the Hartree-Fock band structure [inset of Fig. 4(a)].

We quantify the altermagnetic spin splitting from the spectral function by taking the difference in bandwidths $\Delta_{2\pi/3} = W^A(k_1, 2\pi/3) - W^B(k_1, 2\pi/3)$ along the $(k_1, k_2 = 2\pi/3)$ cut of the two sublattice-resolved spectra, which we find to be numerically more stable than directly extracting the splitting at fixed momenta (see the Supplemental Material [73]). The spin splitting, measured in units of hoppings, increases as J/t increases; see Fig. 4(b). This is understood from the limit of large J/t. There, the confining energy of spinon and holon increases, resulting in shorter strings on average and hence a larger renormalization factor of the free-hole contribution in Eq. (3). Crucially, a Hartree-Fock calculation for the altermagnetic Mott insulator predicts that the splitting is weakly dependent on the ratio of J/t (dashed lines), and it is severely overestimated.

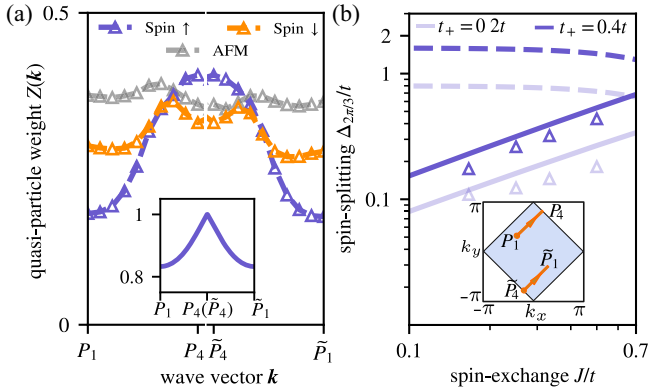


FIG. 4. Spectral signatures of altermagnets. (a) Quasiparticle weight of the polaron branch of the electron spin ↑ (blue) and spin ↓ (orange) spectra for a cut through the Brillouin zone [shown in inset of (b)]. Triangles are tensor network results. For spin ↑, which in the Néel ordered state is mainly affected by the diagonal hopping in the $\boldsymbol{a}_1$ direction, the spectral weight is peaked at $k_1 = \pi(P_4)$, while spin ↓ shows a flatter spectral weight. By contrast, for this cut the antiferromagnetic response has an almost uniform quasiparticle weight. Inset: the spectral weight transfer of the altermagnet can be understood as an interference effect from hopping on our lattice geometry. (b) Spin splitting $\Delta_{2\pi/3}$, as a function of J/t obtained from tensor networks (triangles). Self-consistent Hartree-Fock (dashed lines) strongly overestimates the spin splitting; however, the numerical results agree well with the parton theory (solid lines).

Hence also the spin splitting is strongly renormalized due to the formation of the altermagnetic polaron, and interaction effects are crucial to describe the ARPES spectral function.

Conclusions and outlook—We have developed a theory for the ARPES response of altermagnetic Mott insulators. The spectrum consists of a quasiparticle branch at low energies, which we identify as the altermagnetic polaron. We find that the bandwidth of the altermagnetic polaron and the characteristic spin splitting are strongly renormalized compared with self-consistent Hartree-Fock calculations. A key experimental signature, that we predict in addition to the spin splitting, is the spectral weight transfer between different spin polarizations; see Fig. 1(c). For future work, the parton theory could provide an effective description of altermagnets in the effective Ising limit [81], by extending the conventional anisotropic $t - J_z$ model [63]. On a technical level, the parton theory for the polaron formation can be improved by going beyond the mean-field spinon approximation using variational techniques. Furthermore, it will be interesting to consider realistic band structures for certain insulating altermagnetic candidate materials to quantitatively compare with experiments, as well as multiorbital altermagnetic models [14,82].

Our theory on the altermagnetic polaron provides a systematic study of interaction effects in the ARPES response of altermagnetic Mott insulators and can be directly extended to other spectroscopic probes, such as the spin-polarized scanning tunneling spectroscopy response, where a hole is locally doped into the sample. The model we studied can also be realized in cold-atomic [15], which can provide analogous information to that obtained with ARPES measurements [83,84]. In particular, quantum gas microscopy [85,86] offers a powerful probe of the spectral properties of ultracold atoms, providing complementary and, in some cases, analogous insights to ARPES in solid-state systems. Several experiments have already explored dopant effects and magnetic polaron formation in two-dimensional Fermi-Hubbard antiferromagnets [79,87–89]. Our Letter paves the way for a systematic study of the doping effects in altermagnetic Mott insulators, and may guide further investigations of instabilities of these states toward pair density wave and finite-momentum paired superconductors.

Note added—Recently, we became aware of related work studying the ARPES response of altermagnetic Mott insulators [90]. During the review process, further related works on altermagnetic Mott insulators have appeared [91,92].

Acknowledgments—We thank W. Kadow, J. Knolle, and V. Leeb for insightful discussions. We acknowledge support from the Deutsche Forschungsgemeinschaft (DFG, German Research Foundation) under Germany's Excellence Strategy–EXC–2111–390814868, TRR 360–492547816 and DFG Grants No. KN1254/1-2 and No. KN1254/2-1, the European Research Council (ERC) under the European Union's Horizon 2020 research and innovation program (Grant Agreement No. 851161), the European Union (Grant Agreement No. 101169765), as well as the Munich Quantum Valley, which is supported by the Bavarian state government with funds from the Hightech Agenda Bayern Plus.

Data availability—Data and codes are available upon reasonable request on Zenodo [93].

[1] L. Šmejkal, J. Sinova, and T. Jungwirth, Emerging research landscape of altermagnetism, Phys. Rev. X **12**, 040501 (2022).
[2] L. Šmejkal, J. Sinova, and T. Jungwirth, Beyond conventional ferromagnetism and antiferromagnetism: A phase with nonrelativistic spin and crystal rotation symmetry, Phys. Rev. X **12**, 031042 (2022).
[3] I. I. Pomeranchuk *et al.*, On the stability of a Fermi liquid, Sov. Phys. JETP **8**, 361 (1958).
[4] C. Wu, K. Sun, E. Fradkin, and S.-C. Zhang, Fermi liquid instabilities in the spin channel, Phys. Rev. B **75**, 115103 (2007).
[5] K.-H. Ahn, A. Hariki, K.-W. Lee, and J. Kuneš, Antiferromagnetism in RuO_2 as *d*-wave Pomeranchuk instability, Phys. Rev. B **99**, 184432 (2019).

[6] S. Hayami, Y. Yanagi, and H. Kusunose, Momentum-dependent spin splitting by collinear antiferromagnetic ordering, J. Phys. Soc. Jpn. **88**, 123702 (2019).

[7] L. Šmejkal, R. González-Hernández, T. Jungwirth, and J. Sinova, Crystal time-reversal symmetry breaking and spontaneous Hall effect in collinear antiferromagnets, Sci. Adv. **6**, eaaz8809 (2020).

[8] S. Hayami, Y. Yanagi, and H. Kusunose, Bottom-up design of spin-split and reshaped electronic band structures in antiferromagnets without spin-orbit coupling: Procedure on the basis of augmented multipoles, Phys. Rev. B **102**, 144441 (2020).

[9] I. I. Mazin, K. Koepernik, M. D. Johannes, R. González-Hernández, and L. Šmejkal, Prediction of unconventional magnetism in doped $FeSb_2$, Proc. Natl. Acad. Sci. U.S.A. **118**, e2108924118 (2021).

[10] D.-F. Shao, S.-H. Zhang, M. Li, C.-B. Eom, and E. Y. Tsymbal, Spin-neutral currents for spintronics, Nat. Commun. **12**, 7061 (2021).

[11] L. Šmejkal, A. B. Hellenes, R. González-Hernández, J. Sinova, and T. Jungwirth, Giant and tunneling magnetoresistance in unconventional collinear antiferromagnets with nonrelativistic spin-momentum coupling, Phys. Rev. X **12**, 011028 (2022).

[12] I. Mazin (The PRX Editors), Editorial: Altermagnetism—A new punch line of fundamental magnetism, Phys. Rev. X **12**, 040002 (2022).

[13] T. A. Maier and S. Okamoto, Weak-coupling theory of neutron scattering as a probe of altermagnetism, Phys. Rev. B **108**, L100402 (2023).

[14] V. Leeb, A. Mook, L. Šmejkal, and J. Knolle, Spontaneous formation of altermagnetism from orbital ordering, Phys. Rev. Lett. **132**, 236701 (2024).

[15] P. Das, V. Leeb, J. Knolle, and M. Knap, Realizing altermagnetism in Fermi-Hubbard models with ultracold atoms, Phys. Rev. Lett. **132**, 263402 (2024).

[16] F. Ferrari and R. Valentí, Altermagnetism on the Shastry-Sutherland lattice, Phys. Rev. B **110**, 205140 (2024).

[17] P. d'Ornellas, V. Leeb, A. G. Grushin, and J. Knolle, Altermagnetism without crystal symmetry, Phys. Rev. B **113**, 024426 (2026).

[18] S. He, J. Zhao, H.-G. Luo, and S. Hu, Altermagnetism and beyond in the $t - t' - \delta$ Fermi-Hubbard model, arXiv:2503.08362.

[19] Z. Wu, M. Long, H. Chen, S. Paul, H. Matsuki, O. Zheliuk, U. Zeitler, G. Li, R. Zhou, Z. Zhu, D. Graf, T. I. Weinberger, F. M. Grosche, Y. Maeno, and A. G. Eaton, The Fermi surface of RuO_2 measured by quantum oscillations, Phys. Rev. X **15**, 031044 (2025).

[20] A. Vijayvargia, E. Day-Roberts, A. S. Botana, and O. Erten, Altermagnets with topological order in Kitaev bilayers, arXiv:2503.09705.

[21] R. Jaeschke-Ubiergo, V.-K. Bharadwaj, W. Campos, R. Zarzuela, N. Biniskos, R. M. Fernandes, T. Jungwirth, J. Sinova, and L. Šmejkal, Atomic altermagnetism, arXiv:2503.10797.

[22] T. Sato, S. Haddad, I. C. Fulga, F. F. Assaad, and J. van den Brink, Altermagnetic anomalous Hall effect emerging from electronic correlations, Phys. Rev. Lett. **133**, 086503 (2024).

[23] Y. Liu, S. Shao, S. He, Z. Y. Xie, J.-W. Mei, H.-G. Luo, and J. Zhao, Quantum dynamics in a spin-$\frac{1}{2}$ square lattice $J_1 - J_2 - \delta$ altermagnet, Phys. Rev. B **111**, 245117 (2025).

[24] J. Chang, H. Lu, J. Zhao, H.-G. Luo, and Y. Ding, Energy dispersion, superconductivity, and magnetic fluctuations in stacked altermagnetic materials, Phys. Rev. B **111**, 104432 (2025).

[25] K. Parshukov, R. Wiedmann, and A. P. Schnyder, Topological crossings in two-dimensional altermagnets: Symmetry classification and topological responses, Phys. Rev. B **111**, 224406 (2025).

[26] L. Del Re, Dirac points and topological phases in correlated altermagnets, Phys. Rev. Res. **7**, 033234 (2025).

[27] R. B. Regmi, H. Bhandari, B. Thapa, Y. Hao, N. Sharma, J. McKenzie, X. Chen, A. Nayak, M. El Gazzah, B. G. Márkus, L. Forró, X. Liu, H. Cao, J. F. Mitchell, I. I. Mazin, and N. J. Ghimire, Altermagnetism in the layered intercalated transition metal dichalcogenide $CoNb_4Se_8$, Nat. Commun. **16**, 4399 (2025).

[28] A. D. Vita *et al.*, Optical switching in a layered altermagnet, arXiv:2502.20010.

[29] X. Gong, A. Fakhredine, and C. Autieri, Tunability of the magnetic properties in ni intercalated transition metal dichalcogenide $NbSe_2$, Phys. Rev. B **112**, 184401 (2025).

[30] X. Zhu, X. Huo, S. Feng, S.-B. Zhang, S. A. Yang, and H. Guo, Design of altermagnetic models from spin clusters, Phys. Rev. Lett. **134**, 166701 (2025).

[31] R. Wiedmann, D.-B. Hering, V. Sulaiman, M. R. Walther, K. P. Schmidt, and G. S. Uhrig, Quantum effects in the magnon spectrum of 2D altermagnets via continuous similarity transformations, arXiv:2511.03528.

[32] A. B. Peces and J. Merino, Altermagnetism in an interacting model of kagome materials, Phys. Rev. B **113**, 165143 (2026).

[33] C. Y. Z. J. J. Ni and G. Chang, Competitive orders in altermagnetic chiral magnons, arXiv:2511.03922.

[34] N. Sicheler, R. Raimondi, G. Sangiovanni, and L. D. Re, Optically tunable spin transport in bilayer altermagnetic Mott insulators, arXiv:2508.06938.

[35] J. A. Sobota, Y. He, and Z.-X. Shen, Angle-resolved photoemission studies of quantum materials, Rev. Mod. Phys. **93**, 025006 (2021).

[36] S. Lee, S. Lee, S. Jung, J. Jung, D. Kim, Y. Lee, B. Seok, J. Kim, B. G. Park, L. Šmejkal, C.-J. Kang, and C. Kim, Broken Kramers degeneracy in altermagnetic MnTe, Phys. Rev. Lett. **132**, 036702 (2024).

[37] J. Krempaský *et al.*, Altermagnetic lifting of Kramers spin degeneracy, Nature (London) **626**, 517 (2024).

[38] T. Osumi, S. Souma, T. Aoyama, K. Yamauchi, A. Honma, K. Nakayama, T. Takahashi, K. Ohgushi, and T. Sato, Observation of a giant band splitting in altermagnetic MnTe, Phys. Rev. B **109**, 115102 (2024).

[39] S. Reimers, L. Odenbreit, L. Šmejkal, V. N. Strocov, P. Constantinou, A. B. Hellenes, R. Jaeschke Ubiergo, W. H. Campos, V. K. Bharadwaj, A. Chakraborty, T. Denneulin, W. Shi, R. E. Dunin-Borkowski, S. Das, M. Kläui, J. Sinova, and M. Jourdan, Direct observation of altermagnetic band splitting in CrSb thin films, Nat. Commun. **15**, 2116 (2024).

[40] J. Ding, Z. Jiang, X. Chen, Z. Tao, Z. Liu, T. Li, J. Liu, J. Sun, J. Cheng, J. Liu, Y. Yang, R. Zhang, L. Deng, W. Jing, Y. Huang, Y. Shi, M. Ye, S. Qiao, Y. Wang, Y. Guo, D. Feng,

and D. Shen, Large band splitting in g-wave altermagnet CrSb, Phys. Rev. Lett. **133**, 206401 (2024).
[41] C. Li, M. Hu, Z. Li, Y. Wang, W. Chen, B. Thiagarajan, M. Leandersson, C. Polley, T. Kim, H. Liu, C. Fulga, M. G. Vergniory, O. Janson, O. Tjernberg, and J. van den Brink, Topological Weyl altermagnetism in CrSb, Commun. Phys. **8**, 311 (2025).
[42] O. Fedchenko *et al.*, Observation of time-reversal symmetry breaking in the band structure of altermagnetic RuO_2, Sci. Adv. **10**, eadj4883 (2024).
[43] G. Yang, Z. Li, S. Yang, J. Li, H. Zheng, W. Zhu, Z. Pan, Y. Xu, S. Cao, W. Zhao, A. Jana, J. Zhang, M. Ye, Y. Song, L.-H. Hu, L. Yang, J. Fujii, I. Vobornik, M. Shi, H. Yuan, Y. Zhang, Y. Xu, and Y. Liu, Three-dimensional mapping of the altermagnetic spin splitting in CrSb, Nat. Commun. **16**, 1442 (2025).
[44] R. D. Gonzalez Betancourt, J. Zubáč, R. Gonzalez-Hernandez, K. Geishendorf, Z. Šobáň, G. Springholz, K. Olejník, L. Šmejkal, J. Sinova, T. Jungwirth, S. T. B. Goennenwein, A. Thomas, H. Reichlová, J. Železný, and D. Kriegner, Spontaneous anomalous Hall effect arising from an unconventional compensated magnetic phase in a semiconductor, Phys. Rev. Lett. **130**, 036702 (2023).
[45] O. J. Amin, A. Dal Din, E. Golias, Y. Niu, A. Zakharov, S. C. Fromage, C. J. B. Fields, S. L. Heywood, R. B. Cousins, F. Maccherozzi, J. Krempaský, J. H. Dil, D. Kriegner, B. Kiraly, R. P. Campion, A. W. Rushforth, K. W. Edmonds, S. S. Dhesi, L. Šmejkal, T. Jungwirth, and P. Wadley, Nanoscale imaging and control of altermagnetism in MnTe, Nature (London) **636**, 348 (2024).
[46] I. Gray, Q. Deng, Q. Tian, M. Chilcote, J. S. Dodge, M. Brahlek, and L. Wu, Time-resolved magneto-optical effects in the altermagnet candidate MnTe, arXiv:2404.05020.
[47] A. Hariki, A. Dal Din, O. J. Amin, T. Yamaguchi, A. Badura, D. Kriegner, K. W. Edmonds, R. P. Campion, P. Wadley, D. Backes, L. S. I. Veiga, S. S. Dhesi, G. Springholz, L. Šmejkal, K. Výborný, T. Jungwirth, and J. Kuneš, X-ray magnetic circular dichroism in altermagnetic α-MnTe, Phys. Rev. Lett. **132**, 176701 (2024).
[48] S. Bey, M. Zhukovskyi, T. Orlova, S. Fields, V. Lauter, H. Ambaye, A. Ievlev, S. P. Bennett, X. Liu, and B. A. Assaf, Interface, bulk and surface structure of heteroepitaxial altermagnetic α-MnTe films grown on GaAs(111), arXiv:2504.12126.
[49] G. Cuono, R. M. Sattigeri, J. Skolimowski, and C. Autieri, Orbital-selective altermagnetism and correlation-enhanced spin-splitting in strongly-correlated transition metal oxides, J. Magn. Magn. Mater. **586**, 171163 (2023).
[50] Y. Guo, H. Liu, O. Janson, I. C. Fulga, J. van den Brink, and J. I. Facio, Spin-split collinear antiferromagnets: A large-scale *ab-initio* study, Mater. Today Phys. **32**, 100991 (2023).
[51] I. V. Maznichenko, A. Ernst, D. Maryenko, V. K. Dugaev, E. Y. Sherman, P. Buczek, S. S. P. Parkin, and S. Ostanin, Fragile altermagnetism and orbital disorder in Mott insulator $LaTiO_3$, Phys. Rev. Mater. **8**, 064403 (2024).
[52] C.-C. Wei, X. Li, S. Hatt, X. Huai, J. Liu, B. Singh, K.-M. Kim, R. M. Fernandes, P. Cardon, L. Zhao, T. T. Tran, B. A. Frandsen, K. S. Burch, F. Liu, and H. Ji, $La_2O_3Mn_3Se_2$: A correlated insulating layered d-wave altermagnet, Phys. Rev. Mater. **9**, 024402 (2025).
[53] L. Garcia-Gassull, A. Razpopov, P. P. Stavropoulos, I. I. Mazin, and R. Valentí, Microscopic origin of the magnetic interactions and their experimental signatures in altermagnetic $La_2O_3Mn_3Se_2$, npj Spintronics **4**, 9 (2026).
[54] S. Schmitt-Rink, C. M. Varma, and A. E. Ruckenstein, Spectral function of holes in a quantum antiferromagnet, Phys. Rev. Lett. **60**, 2793 (1988).
[55] C. L. Kane, P. A. Lee, and N. Read, Motion of a single hole in a quantum antiferromagnet, Phys. Rev. B **39**, 6880 (1989).
[56] S. Sachdev, Hole motion in a quantum Néel state, Phys. Rev. B **39**, 12232 (1989).
[57] R. Strack and D. Vollhardt, Dynamics of a hole in the $t-j$ model with local disorder: Exact results for high dimensions, Phys. Rev. B **46**, 13852 (1992).
[58] D. E. Logan and M. P. H. Stumpf, Finite-temperature hole dynamics in the $t-j$ model: Exact results for high dimensions, Europhys. Lett. **43**, 207 (1998).
[59] G. Sangiovanni, A. Toschi, E. Koch, K. Held, M. Capone, C. Castellani, O. Gunnarsson, S. K. Mo, J. W. Allen, H. D. Kim, A. Sekiyama, A. Yamasaki, S. Suga, and P. Metcalf, Static versus dynamical mean-field theory of Mott antiferromagnets, Phys. Rev. B **73**, 205121 (2006).
[60] C. Taranto, G. Sangiovanni, K. Held, M. Capone, A. Georges, and A. Toschi, Signature of antiferromagnetic long-range order in the optical conductivity of correlated systems, Phys. Rev. B **85**, 085124 (2012).
[61] P. Béran, D. Poilblanc, and R. Laughlin, Evidence for composite nature of quasiparticles in the 2d $t-j$ model, Nucl. Phys. B **473**, 707 (1996).
[62] R. B. Laughlin, Evidence for quasiparticle decay in photoemission from underdoped cuprates, Phys. Rev. Lett. **79**, 1726 (1997).
[63] F. Grusdt, M. Kánasz-Nagy, A. Bohrdt, C. S. Chiu, G. Ji, M. Greiner, D. Greif, and E. Demler, Parton theory of magnetic polarons: Mesonic resonances and signatures in dynamics, Phys. Rev. X **8**, 011046 (2018).
[64] F. Grusdt, A. Bohrdt, and E. Demler, Microscopic spinon-chargon theory of magnetic polarons in the $t-j$ model, Phys. Rev. B **99**, 224422 (2019).
[65] A. Bohrdt, E. Demler, F. Pollmann, M. Knap, and F. Grusdt, Parton theory of angle-resolved photoemission spectroscopy spectra in antiferromagnetic Mott insulators, Phys. Rev. B **102**, 035139 (2020).
[66] A. Bohrdt, F. Grusdt, and M. Knap, Dynamical formation of a magnetic polaron in a two-dimensional quantum antiferromagnet, New J. Phys. **22**, 123023 (2020).
[67] P. Wrzosek and K. Wohlfeld, Hole in the two-dimensional Ising antiferromagnet: Origin of the incoherent spectrum, Phys. Rev. B **103**, 035113 (2021).
[68] O. I. Motrunich, Orbital magnetic field effects in spin liquid with spinon Fermi sea: Possible application to $\kappa-(ET)_2Cu_2(CN)_3$, Phys. Rev. B **73**, 155115 (2006).
[69] A. T. Costa, J. C. G. Henriques, and J. Fernández-Rossier, Giant spatial anisotropy of magnon Landau damping in altermagnets, SciPost Phys. **18**, 125 (2025).
[70] N. Kaushal and M. Franz, Altermagnetism in modified Lieb lattice Hubbard model, arXiv:2412.16421.
[71] S. R. White, Density matrix formulation for quantum renormalization groups, Phys. Rev. Lett. **69**, 2863 (1992).

[72] J. Hauschild and F. Pollmann, Efficient numerical simulations with tensor networks: Tensor Network Python (TeNPy), SciPost Phys. Lect. Notes 5 (2018).
[73] See Supplemental Material at http://link.aps.org/supplemental/10.1103/1d1n-cssv for the tight-binding description of spinons, the numerical tensor network simulations and the spin-wave theory of the Heisenberg altermagnet.
[74] A. Auerbach, *Interacting Electrons and Quantum Magnetism* (Springer Science & Business Media, New York, 1998).
[75] W. Kadow, L. Vanderstraeten, and M. Knap, Hole spectral function of a chiral spin liquid in the triangular lattice Hubbard model, Phys. Rev. B **106**, 094417 (2022).
[76] M. P. Zaletel, Roger S. K. Mong, C. Karrasch, J. E. Moore, and F. Pollmann, Time-evolving a matrix product state with long-ranged interactions, Phys. Rev. B **91**, 165112 (2015).
[77] W. F. Brinkman and T. M. Rice, Single-particle excitations in magnetic insulators, Phys. Rev. B **2**, 1324 (1970).
[78] E. Manousakis, String excitations of a hole in a quantum antiferromagnet and photoelectron spectroscopy, Phys. Rev. B **75**, 035106 (2007).
[79] C. S. Chiu, G. Ji, A. Bohrdt, M. Xu, M. Knap, E. Demler, F. Grusdt, M. Greiner, and D. Greif, String patterns in the doped Hubbard model, Science **365**, 251 (2019).
[80] F. Grusdt, Z. Zhu, T. Shi, and E. Demler, Meson formation in mixed-dimensional $t-J$ models, SciPost Phys. **5**, 057 (2018).
[81] V. P. Kravchuk, K. V. Yershov, J. I. Facio, Y. Guo, O. Janson, O. Gomonay, J. Sinova, and J. van den Brink, Chiral magnetic excitations and domain textures of g-wave altermagnets, Phys. Rev. B **112**, 144421 (2025).
[82] M. Vila, V. Sunko, and J. E. Moore, Orbital-spin locking and its optical signatures in altermagnets, Phys. Rev. B **112**, L020401 (2025).
[83] P. T. Brown, E. Guardado-Sanchez, B. M. Spar, E. W. Huang, T. P. Devereaux, and W. S. Bakr, Angle-resolved photoemission spectroscopy of a Fermi–Hubbard system, Nat. Phys. **16**, 26–31 (2019).
[84] A. Bohrdt, D. Greif, E. Demler, M. Knap, and F. Grusdt, Angle-resolved photoemission spectroscopy with quantum gas microscopes, Phys. Rev. B **97**, 125117 (2018).
[85] W. S. Bakr, J. I. Gillen, A. Peng, S. Fölling, and M. Greiner, A quantum gas microscope for detecting single atoms in a Hubbard-regime optical lattice, Nature (London) **462**, 74 (2009).
[86] J. F. Sherson, C. Weitenberg, M. Endres, M. Cheneau, I. Bloch, and S. Kuhr, Single-atom-resolved fluorescence imaging of an atomic Mott insulator, Nature (London) **467**, 68 (2010).
[87] A. Mazurenko, C. S. Chiu, G. Ji, M. F. Parsons, M. Kanász-Nagy, R. Schmidt, F. Grusdt, E. Demler, D. Greif, and M. Greiner, A cold-atom Fermi–Hubbard antiferromagnet, Nature (London) **545**, 462 (2017).
[88] M. Xu, L. H. Kendrick, A. Kale, Y. Gang, C. Feng, S. Zhang, A. W. Young, M. Lebrat, and M. Greiner, A neutral-atom Hubbard quantum simulator in the cryogenic regime, Nature (London) **642**, 909 (2025).
[89] M. L. Prichard, Z. Ba, I. Morera, B. M. Spar, D. A. Huse, E. Demler, and W. S. Bakr, Observation of magnon-polarons in the Fermi-Hubbard model, Nat. Phys. **21**, 1548 (2025).
[90] M. Daghofer, K. Wohlfeld, and J. van den Brink, Altermagnetic polarons, Phys. Rev. Lett. **136**, 146502 (2026).
[91] K. Leraand, K. Mæland, and A. Sudbø, Spin-dependent quasiparticle lifetimes in altermagnets, Phys. Rev. B **113**, 115148 (2026).
[92] I. Park, T. Birol, A. Georges, and R. M. Fernandes, Impact of strong electronic correlations on altermagnets: The case of NiS_2, Phys. Rev. Mater. **10**, 054415 (2026).
[93] L. Lanzini, P. Das, and M. Knap, Zenodo entry for: Theory of angle resolved photoemission spectroscopy of altermagnetic Mott insulators, 10.5281/zenodo.15553362 (2025).

End Matter

Geometric string theory and frozen spin approximation—We describe the dynamics of a single hole in the altermagntic $t-J$ model using a spinon-holon parton description of the magnetic polaron [61–66]. The hole in the altermagnetic background can be described as a bound state of a heavy spinon carrying a spin quantum number and the light holon carrying the charge. The partons are interconnected by geometric strings which we analyze based on the FSA [63,80] where we assume that the motion of the holon does not alter the quantum state of the spins and only displaces them along the string; see Fig. 5(a).

The electron annihilation operator can be written as

$$c_{j,\sigma} = h_j^\dagger f_{j,\sigma}, \tag{A1}$$

where $h_j^\dagger$ is the bosonic holon creation operator and $f_{j,\sigma}$ is the fermionic spinon operator. The physical Hilbert space is composed of all states satisfying

$$\sum_\sigma f_{j,\sigma}^\dagger f_{j,\sigma} + h_j^\dagger h_j = 1 \ \forall \ j. \tag{A2}$$

First, we consider the ground state $|\Psi_0\rangle$ of the $t-J$ model of the altermagnet at half filling. We create a hole at $\boldsymbol{j}^s$ by applying $c_{\boldsymbol{j}^s,\sigma}$. The spinon is located at $\boldsymbol{j}^s$ with spin $\bar{\sigma}$. Hence, we get a state with a spinon and a holon

$$|\boldsymbol{j}^s, \bar{\sigma}, 0\rangle = c_{\boldsymbol{j}^s,\sigma}|\Psi_0\rangle = h_{\boldsymbol{j}^s}^\dagger f_{\boldsymbol{j}^s,\sigma}|\Psi_0\rangle. \tag{A3}$$

At strong coupling ($t \gg J$, i.e., $U \gg t$), we assume the FSA by considering the spinon to be fixed at $\boldsymbol{j}^s$ and determine the fast holon motion. To this end, we can decompose the Hilbert space as, $\mathcal{H} = \mathcal{H}_\Sigma \otimes \mathcal{H}_{\text{spinon}}$. Here, $\mathcal{H}_{\text{spinon}}$ is the space spanned by all the spinon states and $\mathcal{H}_\Sigma$ is the space spanned by all possible strings of the holon departing from

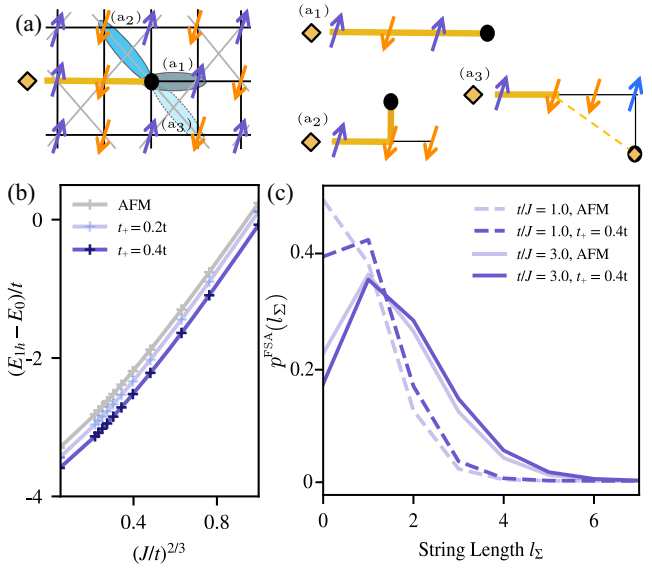


FIG. 5. Spinon-holon parton theory. (a) We illustrate possible holon hopping paths that lead to different spin configurations: the nearest-neighbor hopping t (a_1), which increases the string length by 1 unit and the diagonal hopping t_+ that couples strings of the same length (a_2), or breaks the string and creates a second excitation (a_3). (b) The energy difference for the state with injected hole and the one at half filling scales approximately with $(J/t)^{2/3}$, predicted by the analytical solutions of the single-particle Schrodinger equation. (c) String length distribution for $t/J = 1$ (dotted lines), $t/J = 3$ (solid lines), and $t_+ = 0$ and $t_+ = 0.4t$. With increasing hopping strength, the distribution broadens.

the spinon. The state after creating a string Σ is given by

$$|\boldsymbol{j}^s, \bar{\sigma}, \Sigma\rangle = G_\Sigma h^\dagger_{\boldsymbol{j}^s} f_{\boldsymbol{j}^s,\sigma}|\Psi_0\rangle, \tag{A4}$$

with the string operator

$$G_\Sigma = \prod_{\langle i,j\rangle \in \Sigma} \left(h^\dagger_i h_j \sum_{\tau=\uparrow,\downarrow} f^\dagger_{j,\tau} f_{i,\tau} \right), \tag{A5}$$

where $\langle i, j\rangle$ is along the string Σ. Most of the states $|\boldsymbol{j}^s, \bar{\sigma}, \Sigma\rangle$, which are created in a classical Néel background are orthonormal to each other [64,65]. An exception are so-called Trugman loops, i.e., strings where the holon goes back to its initial position, that change the holon position without additional strings. However, by a counting argument, it can be shown that their effect on the spinon dispersion is small [64]. Further corrections can be obtained by considering self-avoiding walks on the square lattice, which we do not take into account for simplicity [67]. With these approximations, the Hilbert space created by the states $|\boldsymbol{j}^s, \bar{\sigma}, \Sigma\rangle$ has the form of the Bethe lattice (as in the antiferromagnetic case [64]), but now some of the nodes on different branches are interconnected due to the presence of diagonal hopping. In this space, the effective Hamiltonian becomes, $H_{\mathrm{eff}} = H_\Sigma + H_{\mathrm{pot}} + H_{\mathrm{spinon}}$, where the hopping on the sites of the Bethe lattice gives

$$H_\Sigma = -\sum_{\boldsymbol{j}^s,\sigma} \sum_{\langle \Sigma_i, \Sigma_j\rangle} t_{ij} (|\boldsymbol{j}^s, \bar{\sigma}, \Sigma_i\rangle\langle \boldsymbol{j}^s, \bar{\sigma}, \Sigma_j| + \mathrm{H.c.}). \tag{A6}$$

Here, for the strings Σ_i, Σ_j that are separated by nearest neighbors t_{ij} is t, and for strings Σ_i, Σ_j that are separated by a diagonal t_{ij} is $t_+(0)$ in the (1,1) direction and $0(t_+)$ in the $(-1, 1)$ direction for the A (B) sublattice. The motion of the hole creates the string of displaced spins that gives rise to the potential energy given by

$$H_{\mathrm{pot}} = \sum_{\boldsymbol{j}^s,\sigma} \sum_{\Sigma} \langle \boldsymbol{j}^s, \bar{\sigma}, \Sigma|H_J|\boldsymbol{j}^s, \bar{\sigma}, \Sigma\rangle |\boldsymbol{j}^s, \bar{\sigma}, \Sigma\rangle\langle \boldsymbol{j}^s, \bar{\sigma}, \Sigma|. \tag{A7}$$

The tight-binding Hamiltonian of the spinon, H_{spinon}, also appears in the effective Hamiltonian, which involves the exchange of heavy spinons, which we will analyze in the next section. We determine the potential energy $V_{\mathrm{pot}}(\Sigma) = \langle \boldsymbol{j}^s, \bar{\sigma}, \Sigma|H_J|\boldsymbol{j}^s, \bar{\sigma}, \Sigma\rangle$ and its dependence on the string length l_Σ by looking at the correlations among the spins. In a linear approximation, we determine the potential energy as

$$V_{\mathrm{pot}}(\Sigma) = \frac{dE}{dl} l_\Sigma + g_0 \delta_{l_\Sigma,0} + g_1 \delta_{l_\Sigma,1} + E_0, \tag{A8}$$

with $g_0 = -J(C_2 - C_1), g_1 = -J_+(C_2 - C_1)/2, dE/dl = 2J(C_2 - C_1) + J_+(C_1/2 + C_4 - 3C_2/2), E_0 = J(1 + C_2 - 5C_1) + J_+(1/2 - 2C_2)$, where the correlations $C_d = \langle \Psi_0|\boldsymbol{S}_d \cdot \boldsymbol{S}_0|\Psi_0\rangle$ are determined from the undoped ground state $|\Psi_0\rangle$. Here, the sublabel "d" indicates the ordered distance from the other spin we take the correlation with [nearest neighbor $d = 1$, next-nearest neighbor (diagonal) $d = 2$, etc.].

We now motivate the coefficients of the potential energy of strings; first, with our coefficients the $l_\Sigma = 0$ case gives

$$\begin{aligned} V_{\mathrm{pot}}(l_\Sigma = 0) &= g_0 + E_0 \\ &= -J(C_2 - C_1) + J(1 + C_2 - 5C_1) \\ &\quad + J_+(1/2 - 2C_2) \\ &= -J(4C_1 - 1) - J_+(2C_2 - 1/2). \end{aligned} \tag{A9}$$

This result can be checked by calculating the energy cost of removing a particle; see Fig. 6. We also notice that, when expanding on the perfect Neel state, we have $C_2 = C_3 = 1/4$ and $C_1 = C_4 = -1/4$; in this approximation, we get $V_{\mathrm{pot}}(l_\Sigma = 0) = 2J$. We also determine the potential energy of string with length 1:

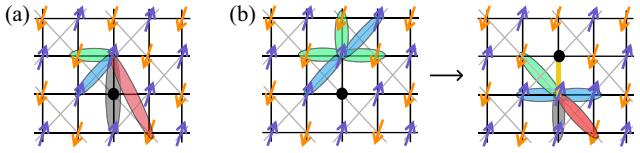


FIG. 6. (a) We highlight NN (C1), N-NN (C2), N-N-NN (C3), and N-N-N-NN (C4) correlations with green, cyan, gray, and red color respectively. In the perfect Néel state, $C_1 = C_4 = -1/4$ and $C_2 = C_3 = 1/4$. (b) The energy cost of a single hole (left) is $E_{l_\Sigma=0} - E_{\mathrm{AFM}} = -4JC_1 - 2J_+C_2 + J + J_+/2 = -J(4C_1 - 1) - J_+(2C_2 - 1/2) = E_0 + g_0$. The energy cost of $l_\Sigma = 1$ (right) is $E_{l_\Sigma=1} - E_{\mathrm{AFM}} = J(1 + 3C_2 - 7C_1) + J_+(1/2 - 4C_2 + C_4 + C_1) = E_0 + g_1 + dE/dl$.

$$\begin{aligned} V_{\mathrm{pot}}(l_\Sigma = 1) &= E_{l_\Sigma=1} - E_{\mathrm{AFM}} \\ &= J(1 + 7C_1 + 2C_2 + C_3) \\ &\quad + J_+(1/2 + C_1 + C_4 - 4C_2) \\ &= E_0 + g_1 + dE/dl = \frac{7J}{2} - J_+ \end{aligned} \tag{A10}$$

[Figure 6(b)], where the last equality holds for the Néel state. To conclude, we determine the dependence of the potential energy on the string length, dE/dl, by analyzing long-string patterns and taking the difference $E_{l_\Sigma+1} - E_{l_\Sigma}$; we show our procedure in Fig. 7.

We numerically determine the ground state (spinon-holon bound state) of the Hamiltonian $H_{\mathrm{pot}} + H_\Sigma$. The ground state is a superposition of strings with probabilities $p_\Sigma^{FSA} = |\psi_\Sigma^{FSA}|^2$, and can be written as

$$|\psi_{\mathrm{FSA}}(\boldsymbol{j}^s, \bar{\sigma})\rangle = \sum_\Sigma \psi_\Sigma^{FSA} |\boldsymbol{j}^s, \bar{\sigma}, \Sigma\rangle. \tag{A11}$$

The probability distributions are plotted in Fig. Fig. 5(c). The linear dependence of the potential on the length of the string leads to the scaling of $E_{\mathrm{FSA}} \sim (J/t)^{2/3}$, which is shown in Fig. 5(b), consistent with the tensor network simulations.

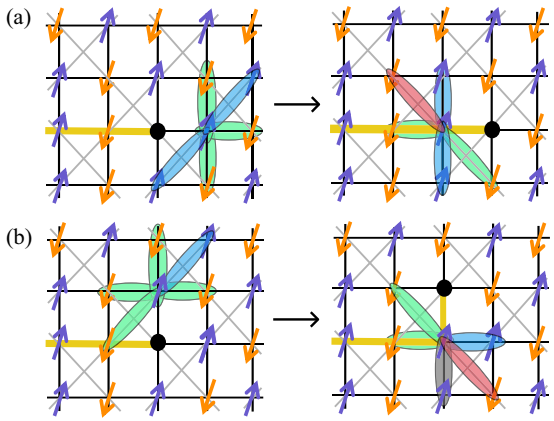


FIG. 7. The holon hops and increases the string length. To calculate (dE/dl), we average between two slightly different cases: (a) the new spin of the string was not interacting with the string before the hopping and (b) the new spin of the string was interacting via a J_+ term with the string. In (a), we get $E_{l_\Sigma+1} - E_{l_\Sigma} = J(2C_2 + C_1 - 3C_1) + J_+(C_4 + C_1 - 2C_2) = 2J(C_2 - C_1) + J_+(C_1 - 2C_2 + C_4)$. In (b), we get $E_{l_\Sigma+1} - E_{l_\Sigma} = J(C_1 + C_3 + C_2 - 3C_1) + J_+(C_4 + C_1 - C_2 - C_1) = 2J(C_2 - C_1) + J_+(C_4 - C_2)$. We average between these two cases and obtain $dE/dl = 2J(C_2 - C_1) + J_+(C_1/2 + C_4 - 3C_2/2)$.

The Hamiltonian $H_{\mathrm{pot}} + H_\Sigma$ considers the spinon to be fixed, whereas H_{spinon} includes the terms that involve the motion of heavy spinons. At $l_\Sigma = 0$, the diagonal hopping does not alter the Néel background, i.e., the potential energy stays the same. This leads to a free-hole behavior in the Néel ordered state, where the spinon and the holon always stay together. We include this contribution in H_{spinon} (see the Supplemental Material [73]), which gives a dispersive contribution to the spectrum.